International Journal of Heat and Fluid Flow 86 (2020) 108726

Contents lists available at ScienceDirect

International Journal of Heat and Fluid Flow

journal homepage: www.elsevier.com/locate/ijhff

Leading edge vortex formation and detachment on a flat plate undergoing simultaneous pitching and plunging motion: Experimental and computational study

Johannes Kissing [a,*], Sebastian Wegt [a], Suad Jakirlic [a], Jochen Kriegseis [b], Jeanette Hussong [a], Cameron Tropea [a]

[a] Institute of Fluid Mechanics and Aerodynamics (SLA), Technical University of Darmstadt, Alarich-Weiss-Straße 10, 64287 Darmstadt, Germany
[b] Institute of Fluid Mechanics (ISTM), Karlsruhe Institute of Technology (KIT), Kaiserstr. 10, 76131 Karlsruhe, Germany

ARTICLE INFO

Keywords:
Unsteady aerodynamics
Leading edge vortex (LEV)
URANS
TR-PIV

ABSTRACT

This study focuses on the formation and detachment of a leading edge vortex (LEV) appearing on an airfoil when its effective angle of attack is dynamically changed, inducing additional forces and moments on the airfoil. Experimental measurements of the time-resolved velocity field using Particle Image Velocimetry (PIV) are complemented by a computational study using an URANS (Unsteady Reynolds-Averaged Navier–Stokes) framework. In this framework a transition-sensitive Reynolds-stress model of turbulence, proposed by Maduta et al. (2018), which combines the near-wall Reynolds-Stress model by Jakirlic and Maduta (2015) and a phenomenological transition model governing the pre-turbulent kinetic energy by Walters and Cokljat (2008), is employed. Combined pitching and plunging kinematics of the investigated flat plate airfoil enable the effective inflow angle to be arbitrarily prescribed. A qualitative assessment of flow fields and a quantitative comparison of LEV characteristics in terms of its center position and circulation as well as an investigation of the mechanism causing the vortex to stop accumulating circulation revealed close agreement between the experimental and simulation results. Further considerations of the lift contribution from the pressure and suction side of the airfoil to the overall lift indicates that the qualitative lift evolution is reproduced even if the pressure side contribution is neglected. This reveals important characteristics of such airfoil dynamics, which can be exploited in future experimental studies, where direct aerodynamic force and moment measurements are greatly inhibited by dominating inertial forces.

1. Introduction

Aerodynamic forces and moments induced by the leading edge vortex (LEV) on airfoils that experience a sudden change in angle of attack are of relevance for a multitude of applications. The induced lift during the growth phase of the LEV is exploited by insects to attain higher lift and is often considered as inspiration for the development of propulsion concepts for Micro Air Vehicles (MAVs) (Eldredge and Jones, 2019). However, in other applications the negative pitching moment on the airfoil during the LEV detachment can endanger the structural integrity of components, for example rotating helicopter blades or wind turbine blades.

Topological flow characteristics on an airfoil experiencing a dynamic change of the inflow angle are described by dynamic stall phenomena (McCroskey, 1982; Carr, 1988; Corke and Thomas, 2015). With an increasing angle of attack, the flow over the airfoil separates and recirculates increasingly earlier until the boundary layer at the leading edge starts to roll up into a LEV. When the angle of attack is further increased, the vortex grows by accumulating mass and circulation transferred from the separated leading-edge shear layer. As long as the vortex is attached to the airfoil, the dynamic lift significantly exceeds the static lift. Depending on the experimental parameters, flow reversal at the trailing edge or an eruption of the boundary layer beneath the vortex leads to vortex detachment (Widmann and Tropea, 2015). Both detachment mechanisms have in common that secondary structures grow on the upper airfoil surface ahead of the main vortex and cut off

* Corresponding author.
E-mail address: kissing@sla.tu-darmstadt.de (J. Kissing).
URL: http://www.sla.tu-darmstadt.de (J. Kissing).

https://doi.org/10.1016/j.ijheatfluidflow.2020.108726
Received 11 June 2020; Received in revised form 24 August 2020; Accepted 28 September 2020
Available online 29 October 2020

the LEV from its feeding shear layer. According to Wu et al. (2006), the dynamic lift is significantly lower than the static lift during and after the detachment phase of the vortex due to the convection of circulation away from the airfoil. Additionally, a negative pitching moment is induced on the airfoil.

The long-term goal of the current project is to increase and prolong the dynamic lift by delaying the leading-edge vortex detachment with the aid of a dielectric barrier discharge (DBD) plasma actuator (Benard and Moreau, 2014; Kotsonis, 2015; Kriegseis et al., 2016). Future numerical studies are intended to identify topologically effective and efficient actuation strategies in terms of actuation strength, timing and location based on a numerical integration of the plasma actuator developed by Maden et al. (2016). Therefore a common numerical and experimental baseline case without an actuator is examined in this study to validate the numerical setup.

However, in the framework of this study – and particularly on the grounds of a direct comparison of numerical simulations and experimental results – the resulting forces induced on the airfoil will be investigated. These investigations address and resolve a very common difficulty encountered with experimental studies of unsteady aerodynamic configurations, especially those conducted in air. In such cases the motion required to achieve a desired reduced frequency, together with the model mass, lead to inordinately high inertial loads acting on the motion actuators, dominating any fluctuations of aerodynamic loads (de Croon et al., 2015), which are those of primary interest. Thus, the aerodynamic loads are typically completely masked in sensor noise. This then hinders a direct experimental comparison between the development of the velocity field and the aerodynamic forces, especially lift and pitching moment.

These forces and moments are difficult to measure with alternative means. Pressure taps on a moving model introduce insurmountable difficulties in terms of oscillating air columns (Cordes, 2016) and moreover, add weight to the model, necessitating even more powerful actuators to achieve a given reduced frequency (Rival and Tropea, 2010).

A further alternative is to deduce forces directly from the measured velocity field, a technique which has been well-established in recent years (DeVoria et al., 2014; Noca et al., 1999; Rival and van Oudheusden, 2017). However, application of this technique requires not only dedicated experimental facilities, but is also quite complex. One major difficulty is that when the velocity field is captured using PIV, both sides of the moving airfoil must be illuminated, unlike the more common one-sided illumination, in which only the suction side of the airfoil is measured and a shadow is cast on the pressure side. Some setups have been introduced using transparent models, through which a laser light sheet can pass from the suction to pressure side or refractive index matching techniques (Budwig, 1994; Rival et al., 2011; Wiederseiner et al., 2011); however, also this leads to model complication and fabrication difficulties.

Also techniques exist in which pressure can be obtained from PIV velocity data, and these do not require information throughout the entire velocity field, as discussed in van Oudheusden (2013). Such techniques have been used to determine hydrodynamic forces on swimming animals, as demonstrated by Dabiri et al. (2014) and Lucas et al. (2017). They potentially offer a solution to obtain at least the lift contribution of the upper airfoil side by pressure integration. However, the lift contribution of the lower airfoil side with conventional PIV measurements remains elusive and the overall lift is generally underestimated by considering only the upper/suction surface.

In the present study a comparison between numerical and experimental results indicates that for the airfoil kinematics investigated, the lift evolution can be qualitatively very well followed by analysis of the suction-side velocity field only. While this might appear obvious, the usefulness of such an approach should not be underestimated, since acquiring data from both sides of the airfoil complicate the experiment significantly.

2. Airfoil kinematics

In this study a flat plate airfoil of 120 mm chord and 6 mm thickness with asymmetric, sharp leading and trailing edges of 30° tip angle, as shown in Fig. 1, is chosen as a generic flow configuration. The sharp leading edge geometry produces a fixed shear layer separation position during the airfoil motion. Rather than cyclic motion, a one-shot downstroke with combined pitching and plunging kinematics is investigated. By adding pitching motion to pure plunging motion, the effective angle of attack of the inflow on the flat plate $\alpha_{\mathrm{eff}}(t)$ can be arbitrarily prescribed by adding a geometric angle of attack $\alpha_{\mathrm{geo}}(t)$ to the angle of attack induced by the plunging motion $\alpha_{\mathrm{plunge}}(t)$. The one-shot kinematics has been recently shown to result in the same velocity field as cyclic motion (Li et al., 2020). The computational study uses the same geometry and kinematics; accordingly, the effective angle of attack history was chosen to be quasi-sinusoidal with 30° amplitude to generate a sinusoidal $\alpha_{\mathrm{geo}}(t)$ evolution according to:

$$\alpha_{\mathrm{eff}}(t) = 30^{\circ}\ \sin\left(\frac{2\pi t}{T}\right) \tag{1}$$

To investigate a flow configuration representative of biological propulsion in terms of dimensionless numbers, the chord based Reynolds number $Re = U_{\infty}c/\nu$ built with the free-stream velocity U_{∞}, the chord of the flat plate c, and the kinematic viscosity ν, was set to 24,000. The reduced frequency $k = \pi c/(U_{\infty}T)$, computed using the motion period of the full cycle T, was set to 0.48, and the Strouhal Number $St = hc/(U_{\infty}T) = 0.1$, was computed using the full stroke height $h = 0.15\ m$. The corresponding evolution of effective and geometric angles of attack can be seen in Fig. 2.

3. Experimental setup

The experimental investigations were conducted in an open return wind tunnel at the Technische Universität Darmstadt, with a test section of cross-section 450 mm × 450 mm. The free-stream turbulence level in the test section was measured to be below 0.3% for the investigated free-stream velocity of $U_{\infty} = 3.33$ m/s. An encoder controlled pitch-plunge apparatus using magnetically driven shafts was used to move the airfoil. The airfoil spanned the entire tunnel width to avoid three-dimensional flow effects. The maximum deviation of acceleration between the prescribed and measured value was always less than 7% for the investigated parameter range. In any case, the actually measured motion was always used in data processing.

The flow field was measured using two-dimensional, two-velocity component (2D2C), time-resolved particle image velocimetry at an image pair acquisition frequency of 1000 Hz. A laser light sheet of 2 mm thickness positioned at a quarter span of the airfoil was produced by a frequency doubled, dual cavity Nd:YLF laser. A Photron© *SA1.1* CMOS camera with a resolution of 1024 × 1024 pixels captured the DEHS seeded flow in a field of view spanning $x/c = 1.2$ in the flow direction and $x/c = 1.2$ in the airfoil plunging direction. DEHS particles of about 1 μm size and a density of 900 kg/m^3 were generated by blowing

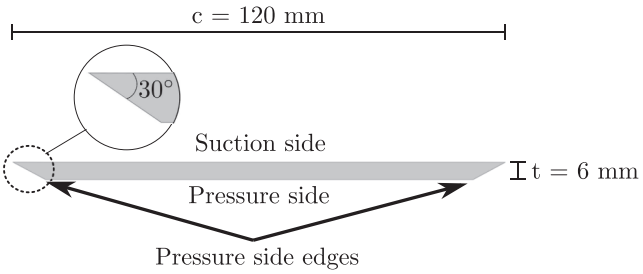

Fig. 1. Flat plate airfoil of 5% thickness with a sharp leading edge (30° tip angle).

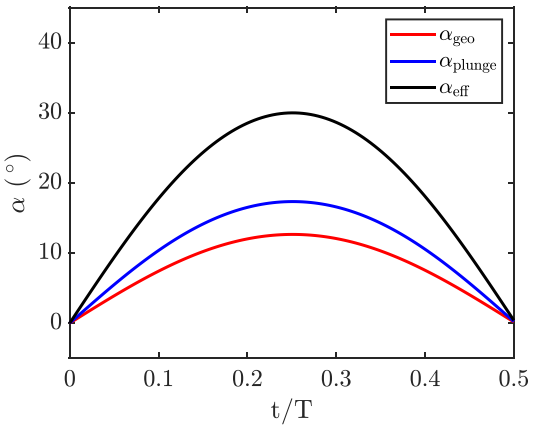

Fig. 2. Evolution of the effective angle of attack α_{eff} introduced by the combined pitching and plunging motion of the airfoil. The geometric angle of attack α_{geo} is added to the induced angle of attack α_{plunge} to α_{eff} for $Re = 24{,}000$, $St = 0.1$ and $k = 0.48$.

pressurized air through 4 Laskin nozzles into a seeding generator from which the aerosol was directed into the settling chamber of the wind tunnel through a seeding rake. Raw images were correlated using a multi-pass, multi-grid interrogation scheme with a final interrogation area (IA) size of 16 × 16 pixels and 50% overlap, providing a resolution of 1.3 mm/IA and 92 velocity values over the chord of the flat plate. A median based outlier filter with a threshold of 2 was used to exclude invalid vectors within a 3 × 3 neighbourhood after the final correlation. The maximum percentage of excluded velocity vectors was always below 3%. Excluded vectors were subsequently interpolated from their respective 3 × 3 neighbourhood.

In order to quantify the leading edge vortex circulation Γ_{LEV} and its center position (x_{LEV} and y_{LEV}), two scalar fields based on the method proposed by Graftieaux et al., 2001 were considered. The vortex center is determined by the maximum of the Γ_1 scalar field and the LEV boundary identified from the Γ_2 scalar fields with a threshold of $\Gamma_2 = 2/\pi$. For this threshold, only regions of pure shear are attributed to the vortex domain. To obtain Γ_{LEV}, the vorticity within the detected Γ_2 boundary was spatially integrated according to Stokes' theorem. Further details on the evaluation of different vortex identification procedures can be found in Kissing et al. (2020). For the investigated parameter set, 10 individual runs were recorded and correlated from which the vortex quantities were extracted on a phase-averaged basis. For all investigated vortex quantities the standard deviation of the phase-averaged characteristics was found to be within 4% of the asymptotic standard deviation computed from 30 runs.

4. Computational method, details

The presently employed RANS model of turbulence represents an extension of the near-wall Reynolds stress model (RSM) proposed by Jakirlic and Maduta (2015), which provides enhanced sensitivity to account for laminar-turbulent transition. This background $\overline{u_iu_j}-\omega^h$ model (with $\omega^h = \varepsilon^h/k; k = 0.5\overline{u_iu_i}$) has been derived from the homogeneous-dissipation-based RSM ($\varepsilon^h = \varepsilon - \nu\partial^2 k/(\partial x_i \partial x_i)$) proposed by Jakirlic and Hanjalic (2002). The modelling approach is based on blending the relevant source terms in the momentum and Reynolds stress ($\overline{u_iu_j}$) equations with those originating from an appropriately modified eddy-viscosity based model (EVM) governing the pre-turbulent kinetic energy k_L (Walters and Cokljat, 2008). The resulting model formulation is designed to predict the onset of the laminar-to-turbulent transition, rather than explicitly modifying the RSM equations in a term-by-term manner. The Reynolds stress tensor originating from the transition EVM (defined via the Boussinesq correlation) changes over to a turbulent one (determined by solving the Reynolds stress equation) automatically, once the turbulent kinetic energy k exceeds its laminar (k_L) counterpart. The model has been thoroughly validated in numerous by-pass transition flow configurations in a range of free-stream turbulence intensities (between 0.18% and 6%) subjected to different external pressure gradients also including cases with separation-induced transition, see Maduta et al. (2018) for more details. The predictive capabilities of the present transition-sensitive RSM have been furthermore illustrated in computing both a baseline flow and a plasma-actuated flow past a plunging NACA 0012 airfoil in Kütemeier et al. (2019).

The model equations are implemented into the code OpenFOAM® with which the present simulations are performed. The OpenFOAM® code represents an open source Computational Fluid Dynamics toolbox utilizing a cell-center-based finite-volume method on in-general unstructured numerical grids and employing the solution procedure based on the PISO procedure for coupling the pressure and velocity fields. The convective terms are discretized by the 2nd-order central differencing scheme (CDS) blended by a very low fraction of the upwind scheme (e.g., the CDS fraction reached up to 97%) implemented in the deferred-correction manner. Such a discretization scheme combination is considered adequate in view of a very fine grid used in the regions with high gradients. The implicit temporal discretization was performed by the three-times-level scheme. The temporal resolution adopted yields a Courant number smaller than 1 over the entire solution domain.

The adequately large flow domain, bounded by the upper and lower wind tunnel walls, accommodating the plunging-pitching plate is meshed using the OpenFOAM® code and its utility 'blockMesh'. An appropriately structured, fully hexahedral grid (Fig. 3) consisting of 100,000 cells in the vertical plane is generated with a grading towards the plate and wind tunnel walls, providing the wall-next computational node situated well in the viscous sublayer with the dimensionless wall distance y^+ being substantially smaller than one for the entire simulation time. Accordingly, the governing equations are integrated to the walls applying the boundary conditions based on the exact asymptotic behavior of the mean flow and turbulence quantities, insuring that the near-wall regions are fully resolved. The feasibility of a two-dimensional URANS computational framework has been preliminary checked in comparison with a three-dimensional one by computing a very relevant flow configuration coping with a plunging NACA 0012 airfoil by using the baseline Reynolds stress model in Kütemeier et al. (2019). The resulting vortex structure patterns as well as evaluated lift coefficients exhibit closest mutual agreement. The present experimental observation supports this behavior detecting no noticeably flow variation over the plate in the spanwise direction. The grid movement and deformation occurring during the pitching-plunging down stroke motion, simulating the experimentally realized movement of the plate, is accounted for by using the technique based on the radial basis function developed by Bos et al. (2013). The experimentally measured inflow velocity ($U_\infty = 3.33$ m/s) and turbulence intensity (0.3%) are prescribed at the inflow plane situated at 0.985 m in front of the flat-plate leading edge.

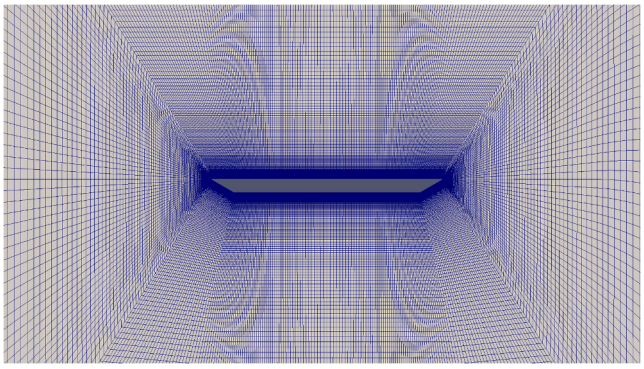

Fig. 3. The numerical grid around the flat plate.

5. Results

Phase-averaged experimental results of the flow field around the flat plate undergoing combined pitching and plunging downstroke motion in terms of normalized vorticity $\omega c/U_\infty$ are shown in Fig. 4(a), (c), (e) and (g) for different dimensionless time instants t/T. The inflow is in the positive x-direction and the airfoil is translated in the negative y-direction. For $t/T = 0.125$ the vortex grows close to the leading edge, attached to the airfoil surface, with the rear flow reattachment point behind the vortex at about $x/c = 0.25$. At this early stage the vortex core consists of concentrated vorticity with a large gradient at its outer boundary. The normalized vorticity attains values of about -40 within the vortex core during this phase of the LEV growth. At $t/T = 0.25$ a counter-rotating secondary vortex arises on the airfoil surface between the vortex and the separated shear-layer at the leading edge. The rear reattachment point behind the vortex reaches the trailing edge at about $t/T = 0.375$, where the vortex center has passed half of the airfoils chord. At this instant the absolute dimensionless peak vorticity value has decreased to about -30. Subsequently, growing secondary structures (secondary and tertiary vortices) ahead of the LEV can be observed, that separate the vortex from its feeding shear layer at $t/T = 0.5$, where the vortex center has travelled downstream of the trailing edge.

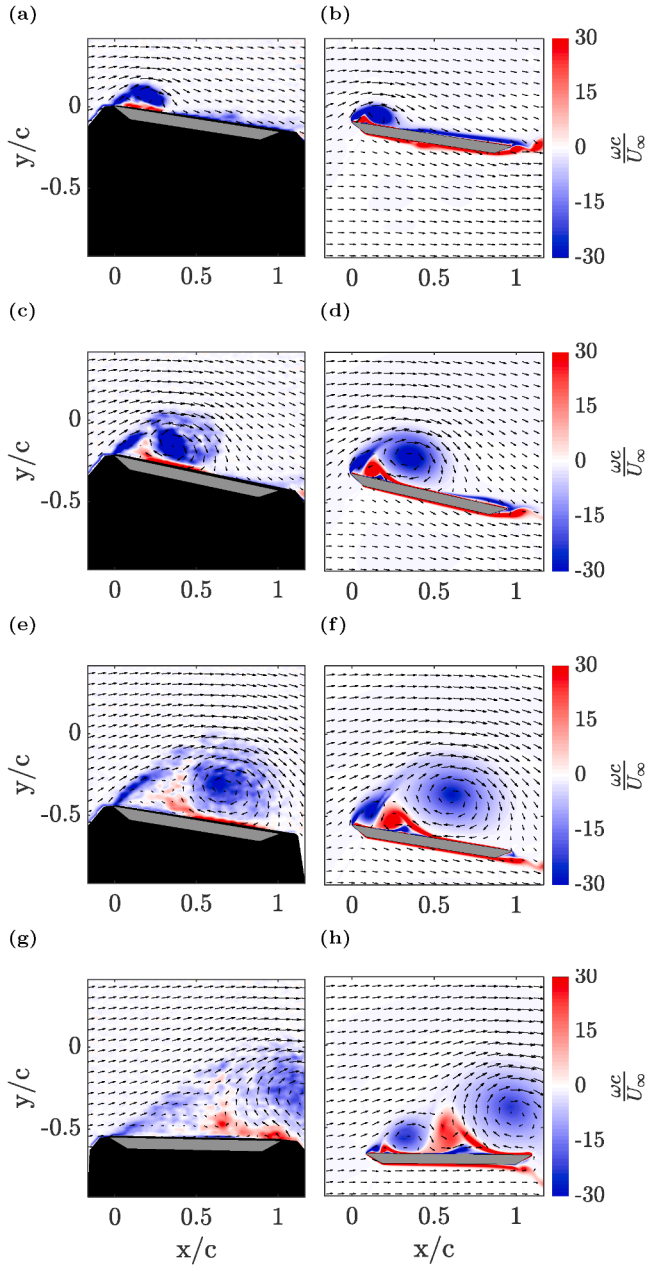

Fig. 4. Time-resolved development of the normalized vorticity field $\omega c/U_\infty$ at $t/T = [0.125\ 0.25\ 0.375\ 0.5]$ for $Re = 24{,}000$, $St = 0.1$ and $k = 0.48$ from PIV measurements in the left column ((a), (c), (e), (g)) and numerical simulations in the right column ((b), (d), (f), (h)).

Fig. 4(b), (d), (f) and (h) illustrates the temporal evolution of the normalized vorticity field obtained from numerical simulations. At the first dimensionless time instant, a concentrated vortex core containing normalized vorticity with values around -40 and the stagnation point of the flow behind the vortex at about $x/c = 0.25$ are in close agreement with the experimental results. The thinner layer of opposite (positive) signed vorticity below the leading edge vortex on the airfoil surface can be attributed to the increased spatial resolution of the numerical results. At $t/T = 0.25$ pronounced secondary structures ahead of the main vortex can be observed, in agreement with experimental results at this instant. The dimensionless time instant at which the rear reattachment point behind the vortex has travelled downstream of the trailing edge ($t/T = 0.375$) is, analogously to the experimental flow fields, accompanied by growing secondary structures that separate the LEV from the leading edge shear layer at $t/T = 0.5$. The absolute dimensionless vorticity peak value at $t/T = 0.375$ is comparable to experimental results at the same time instant.

To quantify the agreement between experiments and simulations in terms of leading-edge vortex characteristics, its circulation Γ_{LEV} was obtained from velocity fields using the vortex identification method proposed by Graftieaux et al. (2001). Fig. 5 shows the comparison of the time-resolved normalized circulation of the LEV obtained by spatial integration of the vorticity within the area detected by the Γ_2 scalar field with a threshold of $\Gamma_2 = 2/\pi$. For the experimentally determined circulation evolution, vortex characteristics were extracted independently from single runs prior to phase averaging. The gray-shaded area indicates the standard deviation from phase averaging in both directions for the experimental results. The computationally obtained normalized circulation evolution follows the experimentally obtained circulation closely up to $t/T = 0.2$. For later non-dimensional time instants, the experimentally determined circulation is lower than the computationally obtained one, with an almost constant offset considering the inherent scatter of the experimental data. Inspection of single frame experimental vortex identification results reveals that the rapid decrease in the experimentally obtained circulation evolution at $t/T = 0.2$ is caused by the fact that the leading edge shear layer is identified as a separate region and not attributed to the main identified vortex from $t/T = 0.2$ onward. However, the LEV keeps accumulating circulation from

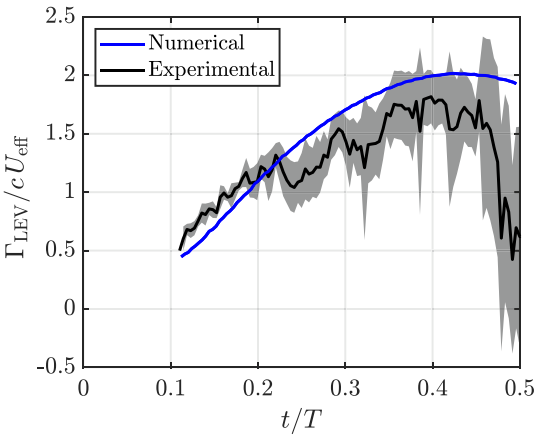

Fig. 5. Comparison of the evolution of the normalized circulation of the leading edge vortex $\Gamma_{LEV}c/U_{eff}$, obtained by spatial integration of the vorticity within the area detected by the Γ_2 scalar field.

the leading edge shear layer. In the vortex identification results from numerical flow fields, the leading edge shear layer and the LEV are identified as connected regions, leading to higher circulation. Based on this, the deviation of circulation evolution, encountered from $t/T = 0.2$ onward, can be attributed to the vortex identification approach used. The peak LEV circulation of both results was detected at about $t/T = 0.4$ with similar normalized circulation values, indicating good temporal and quantitative agreement between numerical simulations and experiments regarding the LEV circulation evolution.

It is interesting to note that the peak circulation occurs shortly after the rear reattachment point of the flow behind the vortex - a half-saddle bound on the airfoil surface from a topological point of view - has travelled downstream of the trailing edge as observed in the flow fields. When this half-saddle convects downstream beyond the trailing edge, fluid from behind the airfoil can recirculate around the trailing edge and become entrained below the main vortex. This fluid contributes to an increased growth of the secondary vortex. The growing secondary vortex in turn can cut off the main LEV from the feeding shear layer, as observed by Rival et al., 2014 and thus, cause its detachment from the airfoil. In order to test this detachment hypothesis for the current experimental parameters, the velocity tangential to the airfoil surface, averaged over the first three velocity values above the airfoil is shown in Fig. 6.

The large negative (blue) diagonal areas in both diagrams are caused by the induced velocity of the clockwise rotating main LEV on the airfoil, which is against the inflow direction. The white strip of zero velocity (marked with a green line) behind the LEV trace of negative velocity, indicates the location on the airfoil where the tangential velocity sign changes, thus indicating the position of the rear reattachment or half-saddle of the flow behind the vortex. When the half-saddle convects downstream of the trailing edge at $x/c = 1$ (marked with a green arrow head), the above-mentioned detachment mechanism is initiated. The experimentally determined trace of the half-saddle reaches the trailing edge at about $t/T = 0.36$ as shown in Fig. 6a, while the numerically obtained half-saddle reaches the trailing edge at about $t/T = 0.38$. The time instant from which fluid can recirculate around the trailing edge occurs just before the corresponding peak LEV circulation is reached. This temporal sequence of fluid recirculation around the trailing edge and subsequent stop of circulation accumulation, in combination with growing secondary vortices, suggest a vortex detachment in accordance with the observations by Rival et al. (2014) for both investigations.

In order to assess the vortex center convection parallel to the airfoil, which, according to Wu et al. (2006), also influences the lift force, the vortex center was computed from the velocity field using the Γ_1 criterion. The center locations were processed for individual experimental runs prior to phase-averaging. Fig. 7 shows the comparison of numerically and experimentally obtained vortex center locations, where the

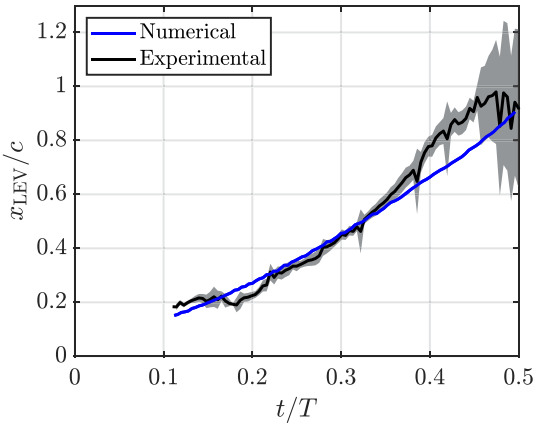

Fig. 7. Comparison of the vortex center x_{LEV} coordinate detected by the Γ_1 criterion. Coordinates are shown in an airfoil-fixed frame of reference.

gray-shaded area indicates the standard deviation of experimental phase averaging. Up to $t/T = 0.3$ both center locations evolve in close agreement, whereas afterwards an increasing divergence of x_{LEV} up to 17% at $t/T = 0.45$ can be observed. Since the vortex was found to detach from its feeding shear layer due to recirculation of fluid around the trailing edge from $t/T = 0.375$ onward, the deviation of its center position occurs at time instants that are no longer in focus for this study or for the overall project. A potential explanation of the deviation is the sensitivity of the vortex topology to small deviations early in the downstroke. Up to $t/T = 0.375$ the deviation of the LEV center position between experiment and simulation was found to be below 10%, which is considered acceptable agreement.

Based on the good agreement of numerical simulation and experimental measurements, numerical results are used to compute the lift contribution of the upper and lower sides of the airfoil to the overall lift. In Fig. 8, the lift coefficients C_l of the suction and pressure side are compared with their sum, which is the overall lift force. These coefficient contributions are obtained by integration of the static surface pressure p along the airfoil according to:

$$C_l = \frac{1}{\frac{\rho_\infty}{2} U_\infty^2 c} \oint_{(C)} p n_y \, dl, \tag{2}$$

where ρ_∞ is the fluid density at the outlet, n_y the component of the normal vector of the surface normal to the free stream velocity, and C the contour around the airfoil section. The integral is implemented as a summation over the available discrete grid points on the plate surface.

Several features of the curves presented in Fig. 8 are noteworthy. For

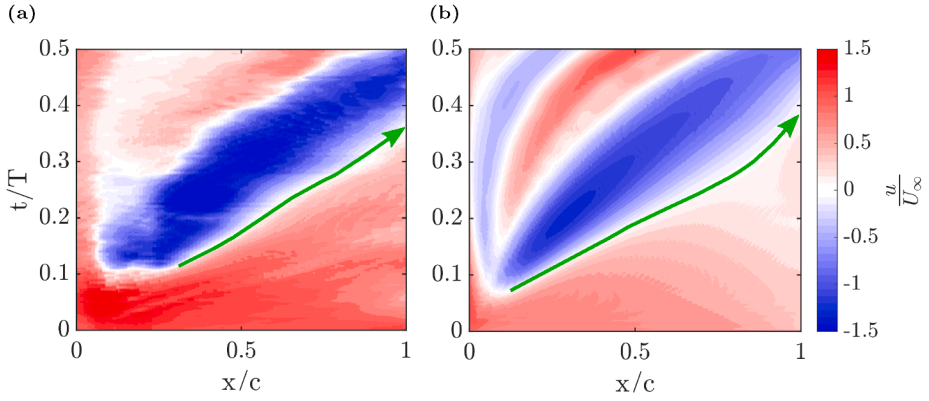

Fig. 6. Evolution of the velocity tangential to the airfoil surface u normalized by U_∞. The trace of the half-saddle behind the LEV is marked with a green line and the instant of recirculation around the trailing edge with an arrow head. (a) Experimental tangential velocity; (b) Numerical tangential velocity. (For interpretation of the references to color in this figure legend, the reader is referred to the web version of this article.)

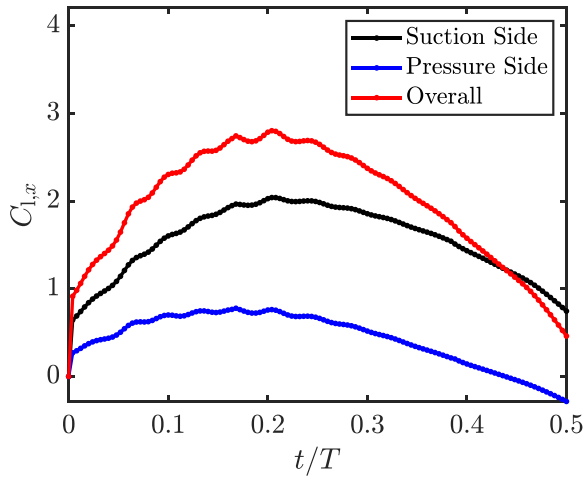

Fig. 8. Normal force coefficient evolution over dimensionless time t/T, divided into contributions from the suction and pressure side of the flat plate. Data come from numerical simulations.

one, the force jumps immediately after motion starts, presumably due to the added mass which must first be accelerated. Thereafter, the force evolution on the upper/suction side corresponds closely to the total force, achieving its maximum at about the same time ($t/T = 0.204$) and differing in magnitude only be the initial offset value. Only after about $t/T = 0.3$ deviations become larger. On the other hand, the pressure side contributes less to the overall force and peaks somewhat earlier ($t/T = 0.168$). The pressure side exhibits also a negative lift force near the end of the motion, accounting for the larger deviation between the upper side contribution and the overall force. It is however apparent, that the change of total lift force throughout much of the plate motion follows very closely the force change on the upper surface, both qualitatively and (with an offset) quantitatively. The consequence of this observation is that measurement of the velocity field development only on the upper side of the plate, should be indicative and correlate well with changes of forces acting on the plate. The contributions coming from the lower surface can be qualitatively neglected, thus simplifying greatly the measurement effort.

To further deepen this insight, the pressure distribution around the plate has been plotted in Fig. 9 for various phases of the motion cycle. The pressure coefficient is computed in the customary manner

$$C_p = \frac{p - p_\infty}{\frac{\rho_\infty}{2} U_\infty^2}, \tag{3}$$

where p_∞ is the reference pressure obtained at the outlet of the computational domain and ρ_∞ is the corresponding density.

The pressure distribution on the upper side, shown in black, exhibits a clear minimum corresponding to the LEV. This vortex induces a velocity on the airfoil surface, with a maximum immediately below the vortex center. This pressure minimum convects towards the trailing edge in subsequent time instants. This agrees well with the movement of the LEV shown in Fig. 7.

On the other hand, the pressure distribution on the pressure side remains almost unchanged at all phases of cycle motion with a linear evolution over chord. Only very small peaks can be detected at $x/c = 0.1$ and 0.9, where the pressure side edges lead to a contour change. These edges are also highlighted in Fig. 1 for orientation. The linear character of the pressure distribution clearly indicates that there are no direct LEV

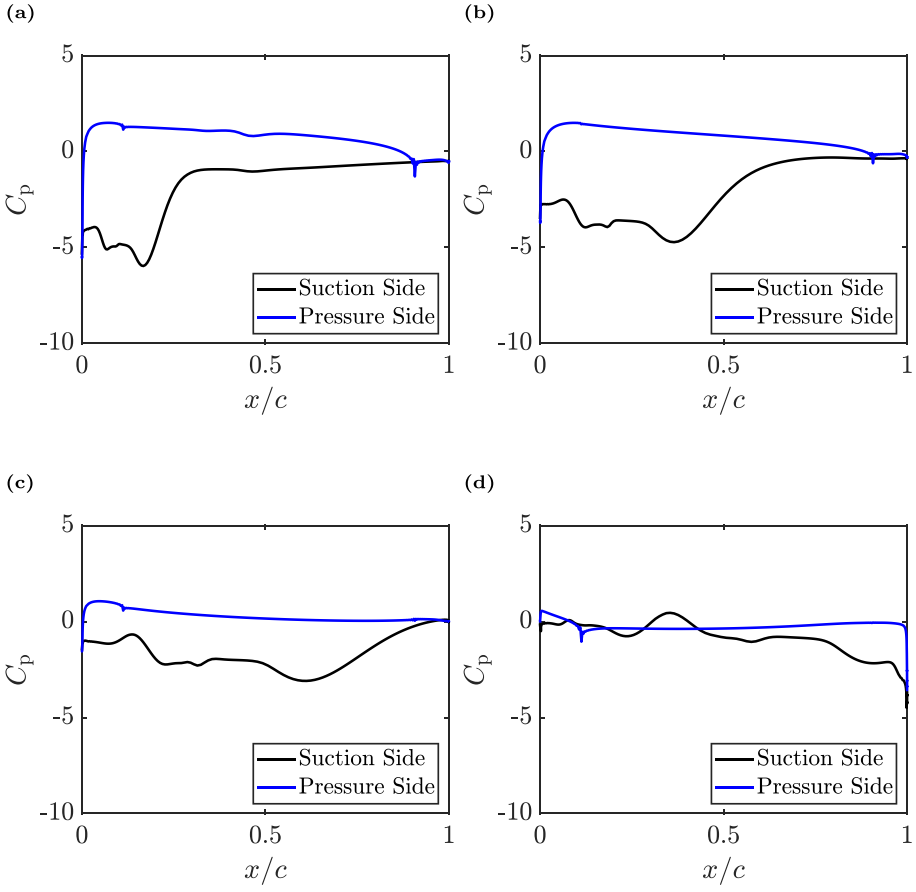

Fig. 9. Surface pressure coefficient C_p over airfoil chord x/c on the pressure and suction side of the airfoil at various phases of the motion cycle: $t/T =$ a) 0.125 b) 0.25 c) 0.375 d) 0.5.

induced pressure effects on the pressure side of the airfoil for the investigated parameters. The conclusion drawn from these observations is concurrent with the remarks associated with Fig. 8, namely that major changes of forces due to the LEV can be to a large extent associated with the velocity field development on the upper side of the plate.

6. Concluding remarks

Comparative numerical and experimental investigations of the leading edge vortex formation and detachment on a pitching and plunging flat plate have shown that computations successfully capture the vortex growth and detachment experimentally obtained using time-resolved particle image velocimetry. Topological flow features in terms of the LEV size and position, as well as the reattachment point of the flow behind the vortex on the airfoil surface and the evolution of secondary structures ahead of the main vortex are in close agreement.

A quantitative assessment of the time resolved LEV circulation and center position evolution with the aid of the Γ_1 and Γ_2 scalar fields has shown that numerical results coincide with experimentally obtained characteristics up to the detachment of the LEV. The vortex peak circulation value and instant, as well as its center position, could be reproduced numerically.

The LEV was found to stop accumulating circulation after the rear reattachment point of the flow behind the vortex has travelled downstream of the trailing edge. This suggests that for the investigated experimental conditions, a recirculation of fluid around the trailing edge initiates the growth of secondary structures that finally cut off the LEV from its feeding shear layer, as reported by Rival et al. (2014). This vortex detachment mechanism is common to both experimental and numerical investigations.

An investigation of the lift contributions from the pressure and suction side of the airfoil to the overall lift force evolution shows that the overall force evolution follows qualitatively closely the suction side contribution. The pressure side is found to contribute only an absolute offset value to the overall lift force. Pressure distribution changes on the suction side of the plate for different phases are found to be dominated by the LEV while the pressure side distribution is not effected by the vortex directly. The generality of following qualitative trends of lift variation based on suction-side flow fields alone has not been shown in the study, although such a capability would be extremely desirable, considering the additional effort required to capture the flow field on both sides of moving airfoils using PIV. With this aim in mind, our studies continue with other airfoils and kinematics, both experimentally and numerically.

CRediT authorship contribution statement

Johannes Kissing: Investigation, Conceptualization, Writing - original draft, Writing - review & editing, Visualization, Project administration. **Sebastian Wegt:** Software, Conceptualization. **Suad Jakirlic:** Methodology, Software, Validation, Supervision. **Jochen Kriegseis:** Conceptualization, Writing - original draft, Writing - review & editing. **Jeanette Hussong:** Funding acquisition, Supervision. **Cameron Tropea:** Conceptualization, Writing - original draft, Writing - review & editing, Supervision, Project administration, Funding acquisition.

Declaration of Competing Interest

The authors declare that they have no known competing financial interests or personal relationships that could have appeared to influence the work reported in this paper.

Acknowledgements

The financial support of the German Research Foundation (DFG) (Grants No. TR 194/55-1 and No. 237267381-TRR150) and Sino-German Center is greatly acknowledged. The authors would like to thank the Lichtenberg HPC at Technical University of Darmstadt for the computing time.

References

Benard, N., Moreau, E., 2014. Electrical and mechanical characteristics of surface ac dielectric barrier discharge plasma actuators applied to airflow control. Experiments in Fluids 55 (11), 360. https://doi.org/10.1007/s00348-014-1846-x.

Bos, F., van Oudheusden, B., Bijl, H., 2013. Radial basis function based mesh deformation applied to simulation of flow around flapping wings. Computers and Fluids 79, 167–177. https://doi.org/10.1016/j.compfluid.2013.02.004.

Budwig, R., 1994. Refractive index matching methods for liquid flow investigations. Experiments in Fluids 17 (5), 350–355. https://doi.org/10.1007/BF01874416.

Carr, L., 1988. Progress in analysis and prediction of dynamic stall. Journal of Aircraft 25 (1), 6–17. https://doi.org/10.2514/3.45534.

Cordes, U., 2016. Experimental investigation of a passively deforming airfoil under dynamic flow conditions. Dissertation, Technische Universität Darmstadt (2016). URL:http://tuprints.ulb.tu-darmstadt.de/5670/.

Corke, T.C., Thomas, F.O., 2015. Dynamic stall in pitching airfoils: aerodynamic damping and compressibility effects. Annual Review of Fluid Mechanics 47 (1), 479–505. https://doi.org/10.1146/annurev-fluid-010814-013632.

Dabiri, J.O., Bose, S., Gemmell, B.J., Colin, S.P., Costello, J.H., 2014. An algorithm to estimate unsteady and quasi-steady pressure fields from velocity field measurements. The Journal of Experimental Biology 217 (Pt 3), 331–336. https://doi.org/10.1242/jeb.092767.

de Croon, G., Perçin, M., Remes, B., Ruijsink, R., de Wagter, C., 2015. The DelFly: Design, Aerodynamics, and Artificial Intelligence of a Flapping Wing Robot, first ed., Springer Netherlands, Dordrecht. doi: 10.1007/978-94-017-9208-0.

DeVoria, A.C., Carr, Z.R., Ringuette, M.J., 2014. On calculating forces from the flow field with application to experimental volume data. Journal of Fluid Mechanics 749, 297–319. https://doi.org/10.1017/jfm.2014.237.

Eldredge, J.D., Jones, A.R., 2019. Leading-edge vortices: mechanics and modeling. Annual Review of Fluid Mechanics 51 (1), 75–104. https://doi.org/10.1146/annurev-fluid-010518-040334.

Graftieaux, L., Michard, M., Grosjean, N., 2001. Combining piv, pod and vortex identification algorithms for the study of unsteady turbulent swirling flows. Measurement Science and Technology 12 (9), 1422–1429. https://doi.org/10.1088/0957-0233/12/9/307.

Jakirlic, S., Hanjalic, K., 2002. A new approach to modelling near-wall turbulence energy and stress dissipation. Journal of Fluid Mechanics 439, 139–166. https://doi.org/10.1017/S0022112002007905.

Jakirlic, S., Maduta, R., 2015. Extending the bounds of 'steady' RANS closures: towards an instability-sensitive reynolds stress model. International Journal of Heat and Fluid Flow 51, 175–194. https://doi.org/10.1016/j.ijheatfluidflow.2014.09.003.

Kissing, J, Kriegseis, J., Li, Z., Feng, L.-H., Hussong, J., Tropea, C., 2020. Insights into leading edge vortex formation and detachment on a pitching and plunging flat plate. Exp Fluids 61, 208. https://doi.org/10.1007/s00348-020-03034-1.

Kotsonis, M., 2015. Diagnostics for characterisation of plasma actuators. Measurement Science and Technology 26 (9). https://doi.org/10.1088/0957-0233/26/9/092001.

Kriegseis, J., Simon, B., Grundmann, S., 2016. Towards in-flight applications? A review on dielectric barrier discharge-based boundary-layer control. Applied Mechanics Reviews 68 (2), 020802. https://doi.org/10.1115/1.4033570.

Kütemeier, D., Wegt, S., Maden, I., Kissing, J., Maduta, R., Kriegseis, J., Jakirlic, S., Tropea, C., 2019. Plasma-actuated lift enhancement of a plunging airfoil: a computational study. AIAA Paper 2019-0305. doi: 10.2514/6.2019-0305.

Li, Z., Feng, L., Kissing, J., Tropea, C., Wang, J., 2020. Experimental investigation on the leading edge vortex formation and detachment mechanism of a pitching and plunging plate. Journal of Fluid Mechanics 901, A17. https://doi.org/10.1017/jfm.2020.509.

Lucas, K.N., Dabiri, J.O., Lauder, G.V., 2017. A pressure-based force and torque prediction technique for the study of fish-like swimming. PloS One 12 (12). https://doi.org/10.1371/journal.pone.0189225.

Maden, I., Maduta, R., Hofmann, J., Jakirlić, S., Kriegseis, J., Tropea, C., Grundmann, S., 2016. Modelling the plasma-actuator-related turbulence production in RANS closures by reference to complementary experimental investigations. Flow, Turbulence and Combustion 97 (4), 1047–1069. https://doi.org/10.1007/s10494-016-9779-5.

Maduta, R., Wegt, S., Jakirlic, S., 2018. A transition-sensitive Reynolds-stress model of turbulence. In: 12th Int. ERCOFTAC Symp. on Engineering Turbulence Modelling and Measurements (ETMM12), Montpellier, France, September 26–28, 2018.

McCroskey, W., 1982. Unsteady airfoils. Annual Review of Fluid Mechanics 14 (1), 285–311. https://doi.org/10.1146/annurev.fl.14.010182.001441.

Noca, F., Shiels, D., Jeon, D., 1999. A comparison of methods for evaluating time-dependent fluid dynamic forces on bodies, using only velocity fields and their derivatives. Journal of Fluids and Structures 13 (5), 551–578. https://doi.org/10.1006/jfls.1999.0219.

Rival, D., Tropea, C., 2010. Characteristics of pitching and plunging airfoils under dynamic-stall conditions. Journal of Aircraft 47 (1), 80–86. https://doi.org/10.2514/1.42528.

Rival, D., Schönweitz, D., Tropea, C., 2011. Vortex interaction of tandem pitching and plunging plates: a two-dimensional model of hovering dragonfly-like flight.

Bioinspiration & Biomimetics 6 (1), 016008. https://doi.org/10.1088/1748-3182/6/1/016008.

Rival, D., Kriegseis, J., Schaub, P., Widmann, A., Tropea, C., 2014. Characteristic length scales for vortex detachment on plunging profiles with varying leading-edge geometry. Experiments in Fluids 55 (1), 37–103. https://doi.org/10.1007/s00348-013-1660-x.

Rival, D.E., van Oudheusden, B., 2017. Load-estimation techniques for unsteady incompressible flows. Experiments in Fluids 58 (3). https://doi.org/10.1007/s00348-017-2304-3.

van Oudheusden, B.W., 2013. PIV-based pressure measurement. Measurement Science and Technology 24 (3). https://doi.org/10.1088/0957-0233/24/3/032001.

Walters, D.K., Cokljat, D., 2008. A three-equation eddy-viscosity model for reynolds-averaged navier–stokes simulations of transitional flow. Journal of Fluids Engineering 130 (12), 121401. https://doi.org/10.1115/1.2979230.

Widmann, A., Tropea, C., 2015. Parameters influencing vortex growth and detachment on unsteady aerodynamic profiles. Journal of Fluid Mechanics 773, 432–459. https://doi.org/10.1017/jfm.2015.259.

Wiederseiner, S., Andreini, N., Epely-Chauvin, G., Ancey, C., 2011. Refractive-index and density matching in concentrated particle suspensions: a review. Experiments in Fluids 50 (5), 1183–1206. https://doi.org/10.1007/s00348-010-0996-8.

Wu, J.-Z., Ma, H.-Y., M.-D. Zhou, Vorticity and Vortex Dynamics, Springer Berlin Heidelberg, Berlin, Heidelberg, 2006. doi:10.1007/978-3-540-29028-5.